

Article

Impeller Design and Performance Analysis of Aviation Fuel Pump Based on the Inverse Method

Chenguang Ping ¹, Jinguang Yang ¹, Michele Ferlauto ^{2,*} and Yang Zhao ³

¹ School of Energy and Power, Dalian University of Technology, Dalian 116024, China; pingcg@163.com (C.P.); jinguang_yang@dlut.edu.cn (J.Y.)

² Department of Mechanical and Aerospace Engineering, Politecnico di Torino, 10129 Turin, Italy

³ Shenyang Blower Works Group Corporation, Shenyang 110869, China; zhaoyang86@shengu.com.cn

* Correspondence: michele.ferlauto@polito.it

Abstract: Centrifugal pumps have a wide range of applications in the aviation field. The present work focuses on the optimal design of aviation fuel pump impellers by means of an inverse method. The fuel pump impeller is designed here by solving an inverse problem, in which the impeller geometry is found by imposing a target blade loading. As the inverse procedure is inviscid, an iterative process based on RANS is then applied to finally converge to a fully viscous solution. Three representative loading distributions have been investigated, and the final performances are evaluated by RANS computations. Since flow variables, rather than the blade geometry, are imposed on the target flow field, it is found that the impellers designed by way of the inverse method have high efficiency under the conditions without cavitation; among them, the pump impeller with a higher loading at the hub maintains a high efficiency for a wide range of flow conditions and also has better anti-cavitation performances under low inlet pressure conditions. Moreover, cavitation resistance can be improved by adjusting the loading distribution near the blade leading edge using the inverse design tool.

Keywords: aviation fuel pump; inverse method; loading distribution; CFD simulation; cavitation

Citation: Ping, C.; Yang, J.; Ferlauto, M.; Zhao, Y. Impeller Design and Performance Analysis of Aviation Fuel Pump Based on the Inverse Method. *Designs* **2023**, *7*, 61. <https://doi.org/10.3390/designs7030061>

Academic Editors: Andrea Magrini, Ernesto Benini

Received: 3 April 2023

Revised: 24 April 2023

Accepted: 28 April 2023

Published: 30 April 2023



Copyright: © 2023 by the authors. Licensee MDPI, Basel, Switzerland. This article is an open access article distributed under the terms and conditions of the Creative Commons Attribution (CC BY) license (<https://creativecommons.org/licenses/by/4.0/>).

1. Introduction

An aviation fuel pump (AFP) is essential for providing fuel to the aero-engine. Among many kinds of pumps, the centrifugal AFP, of which the pressurization is commonly less than 1MPa, is popular due to its high speed, small size, and high reliability. However, there are relatively few studies on the design of centrifugal AFPs [1].

In a centrifugal pump, the impeller is the core component, transferring mechanical energy to the fluid through its rotation. The performance of the pump is directly determined by the performance of its impeller. With the development of computational fluid dynamics (CFD) technology, direct design with optimization based on CFD simulations has become the primary method of impeller design. Westra et al. [2] studied the secondary flow in a centrifugal pump impeller using experimental and CFD techniques, exploring the effects of the Reynolds number and the shape of the inlet profile. Lorusso et al. [3] studied the application of CFD technology in the cavitation simulation of a centrifugal pump. Bozorgasareh et al. [4] studied the effect of a new shroud on pump performance through experiment and numerical simulation. The maturity of CFD technology provides convenience for impeller design and optimization.

In recent years, the inverse problem design of impellers based on loading distribution control has gradually emerged and has been successfully applied to aero-engines. Wang [1] pointed out that the inverse method has good prospects for future application in the design of centrifugal AFPs. The inverse design theory was first proposed by Tan et al. [5]. He explored the influence of factors such as the number of blades, hub-to-tip ratio, and

stacking position on the shape of an axial flow impeller on a simplified meridian flow channel based on the assumptions of infinitely thin blades and incompressible, inviscid fluid. Nowadays, the basic concept of inverse design is mostly derived from this theory. Since then, Borges et al. [6,7] extended this method to the blade design of any meridian flow channel, realized the visualization of the flow field, and verified the feasibility of the design method through experiments. Zangeneh [8] introduced a density term into the governing equations, extending the inverse design theory to compressible fluids. He presented an approximate solution method that ignores the density variation spanwise and an accurate solution method for calculating density in the whole flow channel. Goto et al. [9,10] used the inverse method to optimize a pump diffuser, suppressing the separation flow in the corner region, and proposed a design system for the pump. Based on the inverse design method and CFD technology, combined with the response surface method and simulated annealing method, Daneshkah and Zangeneh [11] investigated the effects of blade loading distribution and stacking conditions on the hydraulic efficiency and cavitation performance of turbine impellers. Oka et al. [12] combined the inverse method with a genetic algorithm, used the pressure rise and adiabatic efficiency as the objective function, and load distribution as variables to optimize the centrifugal compressor impeller, suppressing the flow separation on the suction surface. The inverse design theory has gradually been improved, and its application fields are expanding. However, the main applications still focus on the design and optimization of mainstream impeller machinery, such as compressors, turbines, and water pumps.

In the field of aviation, centrifugal AFP has received significant attention. Dunn et al. [13] studied the difference in cavitation based on different aviation fuels through experiments. Gafurov et al. [14,15] improved the reliability and durability of an AFP by improving the design method and studied the unsteady viscous flow characteristics by using CFD technology. Wang et al. [16] realized the design of a centrifugal AFP by using the velocity coefficient method and explored the influence of different spiral volutes. In recent years, research on AFPs has mainly focused on the effects of cavitation, and there have been relatively fewer studies on relevant design research. Therefore, most of these studies focus on improving cavitation by adding inducers instead of modifying the impellers. However, the inverse design theory provides convenience for studying the cavitation resistance of impellers due to its ability to control the flow field. At present, the direct design based on optimization is still the mainstream design method of AFP impellers, and there is a lack of anti-cavitation research on the impeller itself. This paper adopts inverse design theory and different loading distributions to realize the design of three centrifugal AFP impellers and analyzes the performance of the impellers using CFD technology to investigate the effects of loading distribution on the impeller efficiency and cavitation resistance during the inverse design process.

2. Inverse Design Theory

In the present theory, the fluid is assumed to be steady, inviscid, and incompressible. The numerical procedure imposes a desired feature, e.g., an optimal blade loading distribution, on the flow, whereas the velocity field is constrained to satisfy the tangent condition on the blade surface. So, the core idea of inverse design theory is to iteratively solve the flow field and blade profile on a given meridian flow channel constructed through Bezier curves (Figure 1) so that the impeller blade direction matches the flow direction and finally obtains the impeller geometry that meets the design requirements.

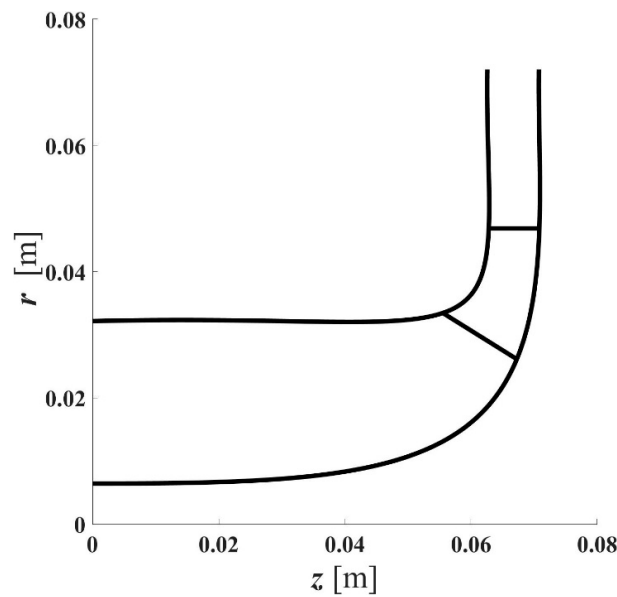


Figure 1. Sketch of the AFP meridian flow channel.

Let us define the angle coordinate α as the difference between the angle coordinate θ and the wrap angle f . The above-mentioned constraint between the velocity field and blade surface can be expressed as:

$$\mathbf{W} \cdot \nabla \alpha = 0 \quad (1)$$

When solving for the flow field, the absolute velocity is decomposed into a mean velocity $\bar{\mathbf{V}}$ and a periodic velocity \mathbf{v} [5]. The relative velocity \mathbf{W} in (1) is therefore defined as $\mathbf{W} = (\bar{V}_r + v_r, \bar{V}_\theta + v_\theta - \omega r, \bar{V}_z + v_z)$.

The solution to the inverse problem will revolve around (1). The velocity field governing equations are derived from the continuity equation, the expression of vorticity, and the Clebsch formulation [5].

2.1. Mean Velocity

In fluid mechanics, the mean velocity components are defined in terms of a stream function Ψ [17] and can be obtained in the cylindrical coordinate system through the formulas:

$$\bar{V}_r = -\frac{1}{rB_f} \frac{\partial \Psi}{\partial z} \quad (2)$$

$$\bar{V}_z = \frac{1}{rB_f} \frac{\partial \Psi}{\partial r} \quad (3)$$

where B_f is the blocking coefficient considering the blade thickness:

$$B_f = 1 - \frac{t_\theta}{r} \frac{B}{2\pi} \quad (4)$$

The B is the number of blades, and t_θ is the tangential thickness of the blade:

$$t_\theta = t_n \sqrt{1 + r^2 \left[\left(\frac{\partial f}{\partial r} \right)^2 + \left(\frac{\partial f}{\partial z} \right)^2 \right]} \quad (5)$$

The expression of vorticity $\bar{\boldsymbol{\Omega}}$ is as follows [5]:

$$\bar{\boldsymbol{\Omega}} = \nabla \times \bar{\mathbf{V}} = \nabla r \bar{V}_\theta \times \nabla \alpha \quad (6)$$

The governing Equation (7) that the Ψ satisfies can be derived by bringing (2) and (3) into (6):

$$\frac{\partial^2 \Psi}{\partial r^2} + \frac{\partial^2 \Psi}{\partial z^2} - \frac{1}{r} \frac{\partial \Psi}{\partial r} + \frac{\partial \Psi}{\partial r} \frac{\partial}{\partial r} \ln \frac{1}{B_f} + \frac{\partial \Psi}{\partial z} \frac{\partial}{\partial z} \ln \frac{1}{B_f} = -r B_f \left(\frac{\partial}{\partial r} r \bar{V}_\theta \frac{\partial f}{\partial z} - \frac{\partial}{\partial z} r \bar{V}_\theta \frac{\partial f}{\partial r} \right) \quad (7)$$

2.2. Periodic Velocity

The periodic velocity can be obtained by calculating the Clebsch formulation [5]:

$$\mathbf{v} = \nabla \Phi(r, \theta, z) - S(\alpha) \nabla r \bar{V}_\theta \quad (8)$$

where $\Phi(r, \theta, z)$ is the potential function of the periodic velocity, and $S(\alpha)$ is the periodic sawtooth function. The Fourier series expressions of $\Phi(r, \theta, z)$ and $S(\alpha)$ in tangential direction are shown to be:

$$\Phi(r, \theta, z) = \sum_{n=-\infty}^{\infty} \Phi_n(r, z) e^{inB\theta} \quad (9)$$

$$S(\alpha) = Re \sum_{n=-\infty}^{\infty} \frac{e^{inB\alpha}}{inB} \quad (10)$$

The periodic velocity satisfies the continuity equation:

$$\nabla \cdot \mathbf{v} = 0 \quad (11)$$

Unlike the governing Equation (7) constructed by vorticity expression, the governing equation of the potential function is derived from the continuity equation of periodic velocity [6]. Bringing (8) into (11), then replacing the relevant terms with (9) and (10), the n th harmonic governing equation of potential function is as follows:

$$\frac{\partial^2 \Phi_n}{\partial r^2} + \frac{\partial^2 \Phi_n}{\partial z^2} + \frac{1}{r} \frac{\partial \Phi_n}{\partial r} - \frac{n^2 B^2}{r^2} \Phi_n = \frac{e^{-inBf}}{inB} \nabla^2 r \bar{V}_\theta - e^{-inBf} \left(\frac{\partial}{\partial r} r \bar{V}_\theta \frac{\partial f}{\partial r} + \frac{\partial}{\partial z} r \bar{V}_\theta \frac{\partial f}{\partial z} \right) \quad (12)$$

2.3. Blade Geometry

By discretizing and solving the governing Equations (7) and (12), the stream function and potential function can be obtained, then the mean velocity $\bar{\mathbf{v}}$ and periodic velocity \mathbf{v} at each node of a grid can also be obtained.

Finally, bringing $\bar{\mathbf{v}}$ and \mathbf{v} into (1), we have

$$(\bar{V}_{rbl} + v_{rbl}) \frac{\partial f}{\partial r} + (\bar{V}_{zbl} + v_{zbl}) \frac{\partial f}{\partial z} = \frac{r \bar{V}_\theta}{r^2} + \frac{v_{\theta bl}}{r} - \omega \quad (13)$$

from which the blade geometry can be deduced. The v_{bl} is the average value of the periodic velocity on both sides of the blade.

3. Design of AFP Impellers Using the Inverse Method

An inverse method design program (IMDP) has been written based on the theory explained in Section 2. The flow chart of the IMDP solution procedure is shown in Figure 2a. The complete design process of an impeller is presented in Figure 2b. After the determination of the design parameters and the physical properties of a working fluid, a specific meridian flow channel and several initial parameters, such as the loading distribution, are imported into IMDP and solved iteratively to obtain an impeller geometry. Then the impeller performance parameters are obtained through CFD simulation using the Reynolds Averaged Navier–Stokes (RANS) method. Based on these parameters, the flow channel or initial parameters can be adjusted, and the process is repeated until the performance of the impeller meets the design requirements. The main

input items required for IMDP include a meridian flow channel, mass flow rate, head, rotational speed, physical property parameters, blade thickness distribution, and load distribution. Among them, the adjustability of the meridian flow channel and load distribution is relatively strong and has a greater impact on the impeller. A meridian flow channel is the basis of inverse design. The channel matching the design parameters can improve the performance of the impeller, and the application of Bezier curves in the flow channel provides a possibility for flexible adjustment. The influence of loading distributions on the impeller will be investigated in this paper.

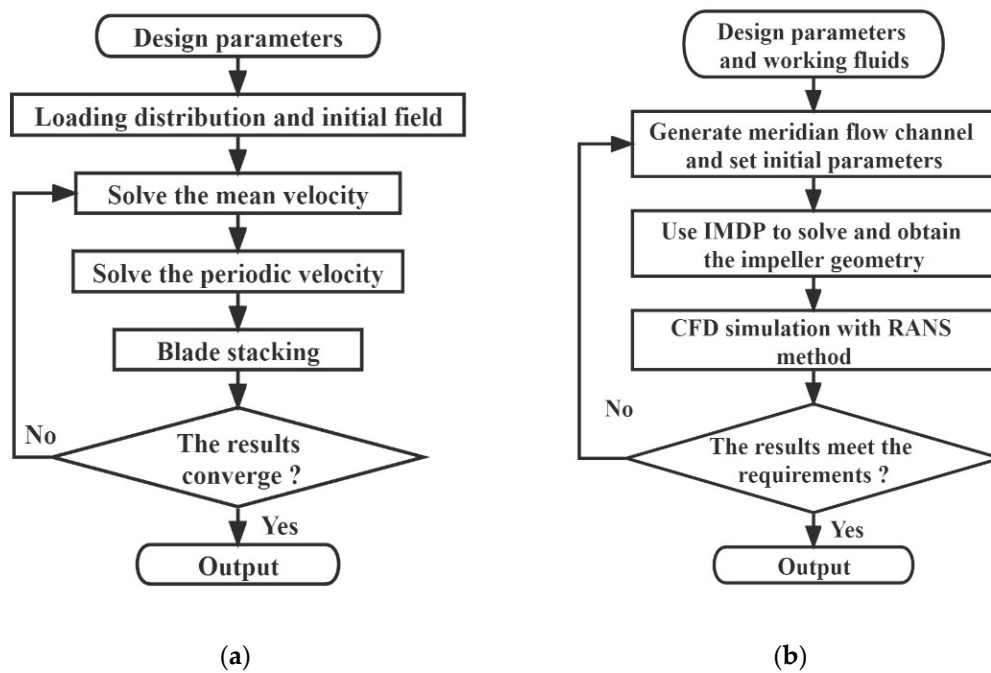


Figure 2. Flow charts of the inverse technique: (a) IMDP calculation; (b) complete design process.

During the operation of the centrifugal impeller, a pressure difference will be formed between the pressure side and the suction side. The pressure difference on both sides of the blade reflects the size of the local work done. The pressure difference of the incompressible fluid has the following expression [18]:

$$p^+ - p^- = \frac{2\pi}{B} V_{bl} \frac{\partial r \bar{V}_\theta}{\partial m} \quad (14)$$

where p^+ and p^- are the pressure on the pressure side and suction side of the blade respectively. V_{bl} is the pitchwise mean meridional velocity. m is the streamwise meridional coordinate.

The main advantage of the inverse method with respect to the direct one is that fluid dynamic constraints can be easily imposed. In this case, a target blade loading can be imposed in order to control the pressure distribution on the blade and obtain the desired performances, then the blade geometry is deduced by running IMDP.

The blade loading mentioned above is the partial derivative of the product of the radius r and the tangential mean velocity \bar{V}_θ on the streamwise meridional coordinate m :

$$\lambda = \frac{\partial r \bar{V}_\theta}{\partial m} \quad (15)$$

The relationship between the blade loading and the impeller head is

$$\omega \int \frac{\partial r \bar{V}_\theta}{\partial m} d m = gH \quad (16)$$

That means one can specify a normalized blade loading distribution which is scaled according to the requested impeller head [19].

In the present work, three representative loading distributions [18,20] are selected for the design of AFP impellers and investigated. These distributions are specified in terms of the control points of the non-uniform rational basis splines (NURBS) (Figure 3). Among them, the first loading distribution (shroud-loading, Figure 3a) should enhance the blade ability near the leading edge and shroud. At the same time, the distribution is beneficial to balance the pressure difference near the trailing edge and has the effect of suppressing the secondary flow under large flow conditions. The second distribution (mid-loading, Figure 3b) is a classical loading distribution. The middle part of the blade is the main work area, while the blade near the leading edge does less work. The last loading distribution (hub-loading, Figure 3c) enhances the ability of the leading edge near the hub, while the shroud side does less work, and the distribution near the trailing edge is similar to the shroud-loading distribution.

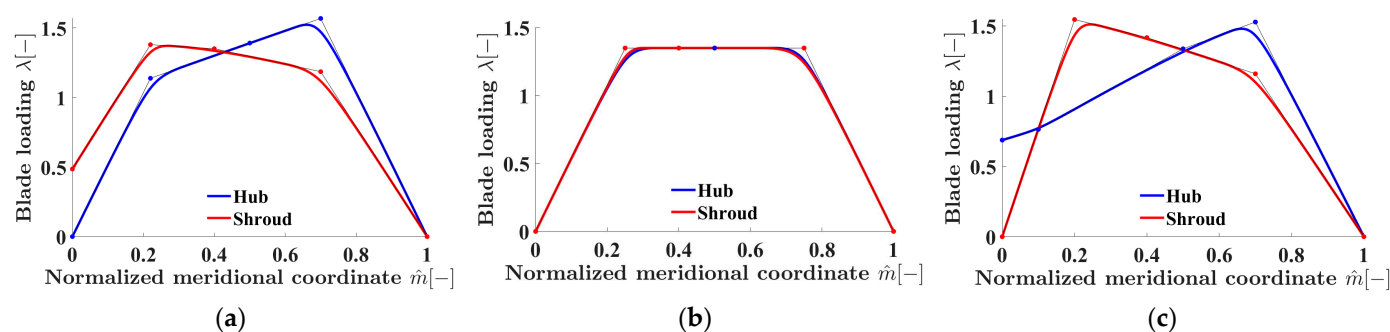


Figure 3. Plots of three representative blade loadings: (a) Shroud-loading distribution; (b) Mid-loading distribution; (c) Hub-loading distribution.

Focusing on the working fluid, i.e., the fuel, it must be observed that the composition of aviation fuels is very complex, usually consisting of thousands of components. Thus, the research on a fuel substitution model based on experimental data has gradually emerged, which greatly facilitates experimental and simulation studies by approximating the aviation fuel's physical properties through the combination of several typical compounds. The fuel model selected in this paper refers to the research of Xiong et al. [21]. The physical parameters (Table 1) are obtained by NIST Refprop.

Table 1. Physical properties of the AFP fuel model.

	Units	Values
T_{em}	°C	20
p_v	Pa	1379
ρ	kg/m ³	746.96
C_p	kJ/(kg•K)	2.125
μ_D	Pa•s	9.9×10^{-4}

Finally, the target values for the design parameters are shown in Table 2. A typical result of the solution of the described numerical IMDP procedure is the impeller geometry, as shown in Figure 4.

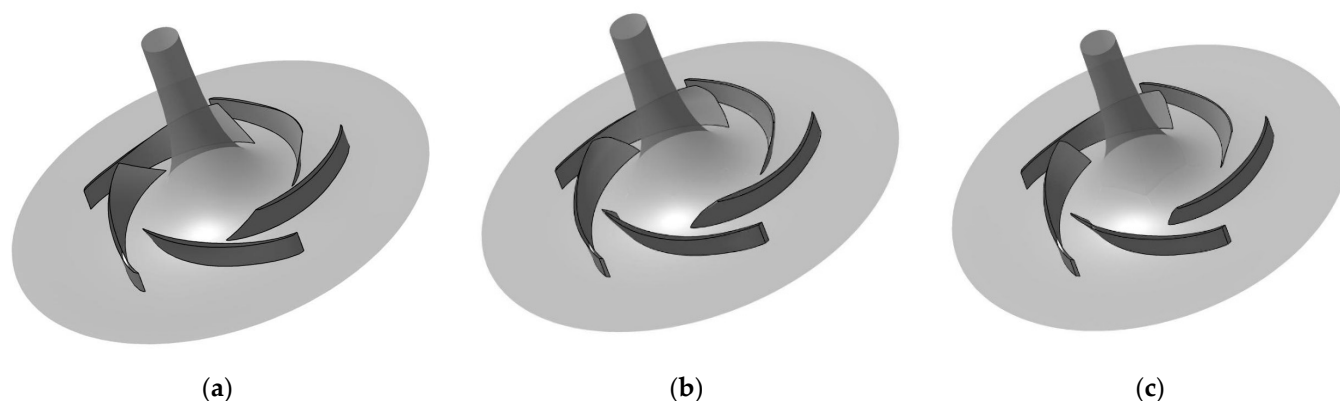


Figure 4. Computed impeller geometries for the different representative loadings: (a) Shroud-loading impeller; (b) Mid-loading impeller; (c) Hub-loading impeller.

Table 2. Design parameters of the AFP impeller.

Flow rate	Rotational Speed	Head
58 m ³ /h	10,000 rpm	82 m

4. CFD Simulation with RANS Method

4.1. CFD Method

The IMPDP procedure generates an impeller geometry solution that does not take into account viscous effects. According to the design process illustrated in Figure 2b, actual performances are then evaluated by a RANS solver. If the check is unsuccessful, the control parameters are modified accordingly, and a new solution is sought by the IMPDP solver. The commercial software Numeca is used to simulate the steady flow in the AFP impeller. The RANS approach with a $k-\epsilon$ turbulence model was selected for the simulation, whereas the barotropic cavitation model is used for cavitation conditions [22].

Concerning the boundary conditions (Figure 5), the velocity is specified at the inlet, and the static pressure is specified at the outlet. The no-slip condition is applied on solid walls that are also considered adiabatic. Periodic boundary conditions are imposed in the peripheral direction.

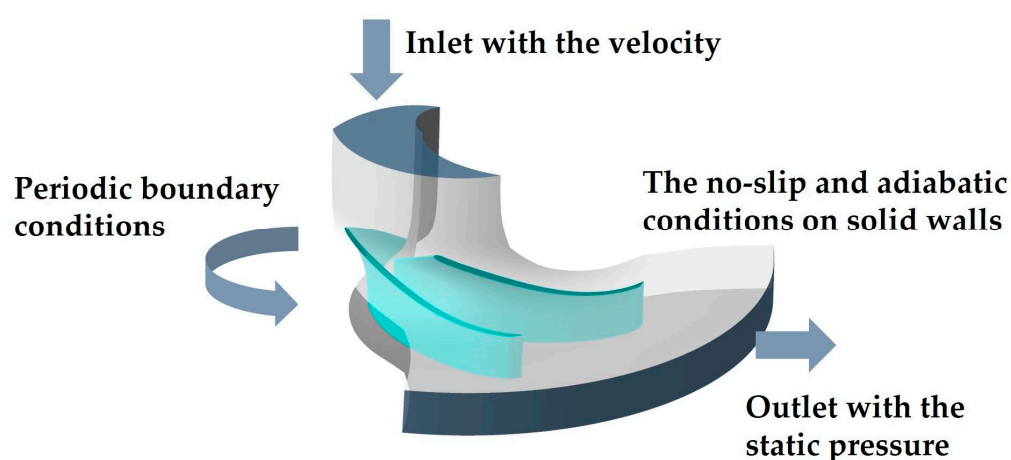


Figure 5. Boundary conditions applied to the impeller CFD calculations.

4.2. The Validation of CFD Simulations

To check the accuracy of the CFD simulation setup and with the aim of finding the optimal grid resolution required for our analyses, the flow over a reference impeller of known geometry, defined as (IMP-0), has been investigated numerically by using different grids. Three-dimensional steady numerical simulations are carried out under various flow conditions.

The hexahedral mesh of IMP-0 is generated by AutoGrid5. The 3D view of the grid on the blade is shown in Figure 6. The mesh quality satisfies orthogonality $> 18^\circ$, elongation ratio < 2.6 , and the first layer of mesh distance is adjusted to make the blade y^+ less than 3. The aim of this grid refinement study is also to identify a good compromise between accuracy and computational costs. The results of the grid sensitivity study are shown in Figure 7a. It is found that the efficiency change does not exceed 0.013%, and the head change does not exceed 0.34% when the number of grids increases from 58k nodes to 163k nodes. Thus, it is considered that the grid with 58k nodes meets the grid independence requirement.

The performance parameters obtained through RANS calculation are compared with the reference data provided by the manufacturer. Figure 7b shows the efficiency and head distribution of IMP-0 over a flow rate ranging from 0.7 to 1.35 times the design flow rate. The efficiency and the head of RANS calculation are in close agreement with the reference data, being a maximum deviation of efficiency of less than 1.4%. Therefore, it is considered that the simulation results have acceptable accuracy and that the above CFD setting can be used for further simulations.

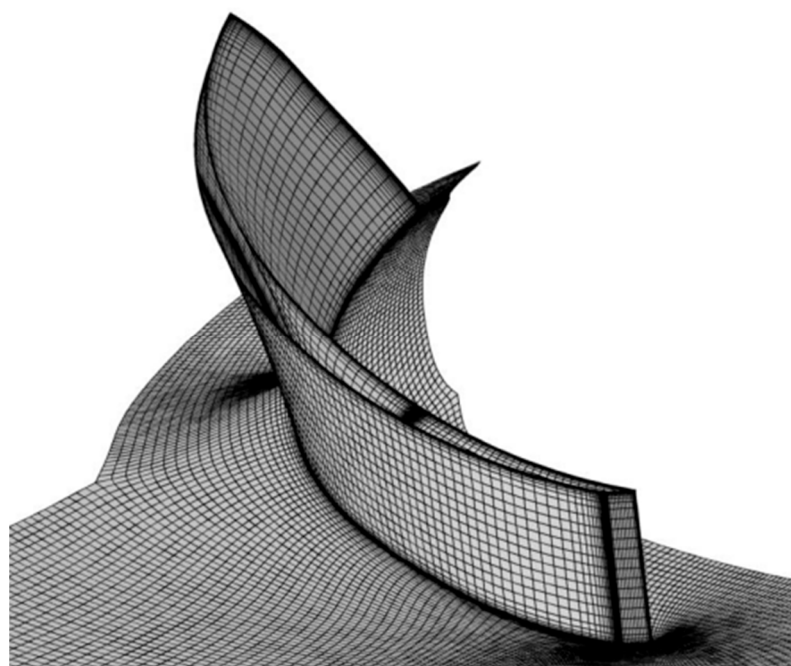


Figure 6. D view of IMP-0 grid.

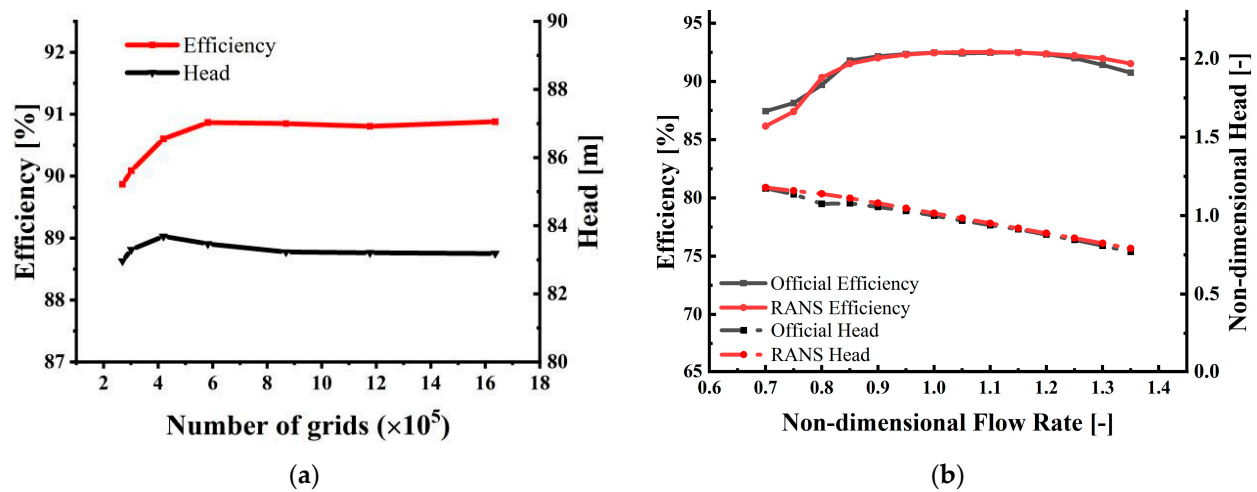


Figure 7. The IMP-0 Impeller test-case. (a) Grid independence study; (b) Performance comparison with manufacturer data.

5. Simulation Results and Performance Analysis

In this section, the results of the IMPDP procedure and the complete design process are discussed. The blade loadings presented in Figure 3 and the target design parameters of Table 2 are applied to the IMPDP procedure. The solution of the inverse problems is found on a 220×33 computational grid by the IMPDP solver, which takes about 31 s for nine iterations to converge. In IMPDP, the geometric convergence will be judged when the variation rate between the average blade wrap angle \bar{f} and the previous calculation result is within 0.5% three times. Figure 8 shows the average blade wrap angle variation rate with the number of iterations.

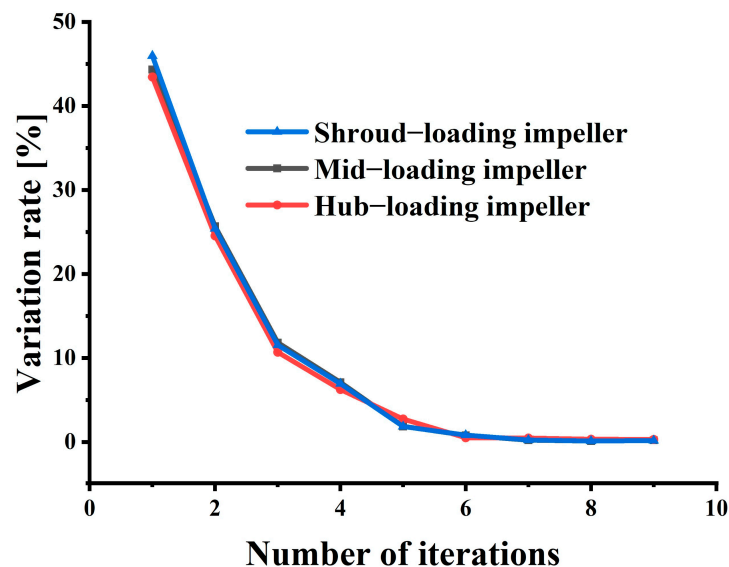


Figure 8. The variation rate of \bar{f} with the number of iterations.

The viscous solution is then computed by the RANS solver on a grid of 58k nodes with the setup obtained by the grid convergence described in the previous section. The computational cost of the RANS simulation takes some minutes on a typical Intel Xeon-based workstation. Moreover, in the process of impeller improvement, only a few parameters need to be changed, and therefore the IMPDP/RANS solvers start from the

previous solution to get a new impeller quickly, which greatly simplifies and speeds up the design process.

At convergence, the IMDP procedure gives both the impeller geometry and the corresponding flow and pressure fields. Figures 9 and 10 show a comparison of the mean velocity and static pressure distributions of the mid-loading impeller on the meridional plane calculated by IMDP and by the RANS method, respectively. The higher mismatch is visible in the comparison of the two velocity fields (Figure 9), as expected. The pressure field, anyway, shows a good agreement between the inviscid and viscous solution (Figure 10), thus confirming the ability of the IMDP approach to correctly capture the pressure field, which lays a foundation for the design of impeller geometries.

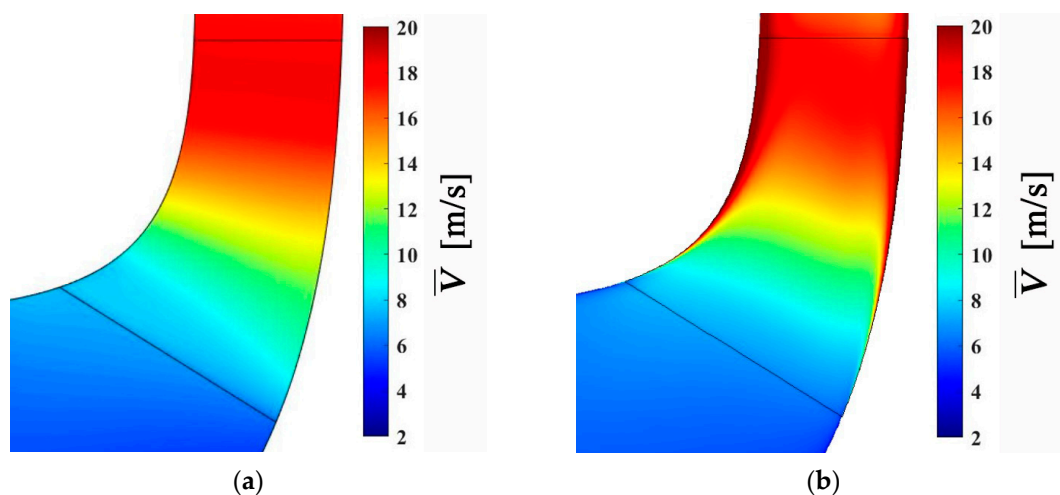


Figure 9. Mean velocity contour of mid-loading impeller: (a) IMDP result; (b) RANS result.

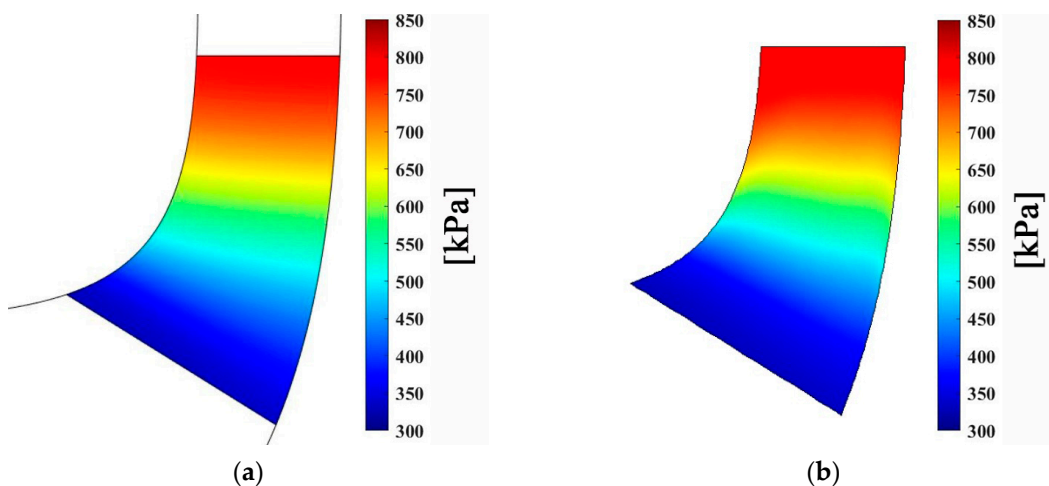


Figure 10. Static pressure contour of mid-loading impeller: (a) IMDP result; (b) RANS result.

Figure 11 shows the relative velocity streamlines calculated by the RANS method at 10% span, 50% span, and 90% span of the mid-loading impeller. The streamlines from the hub side to the shroud side are relatively smooth and consistent with the bending direction of the blades, which is attributed to the idea of calculating the blade geometry based on the flow field in the inverse design theory. The impeller designed based on the inverse method has a good flow field, which means the inverse method can also be applied to flow field optimization and impeller improvement. A performance analysis of all three AFP impellers' designs is then carried out. The performance with variable flow rates under high inlet pressure conditions, the anti-cavitation performance at the design

speed, and the flow rates under low inlet pressure conditions are investigated through CFD simulations.

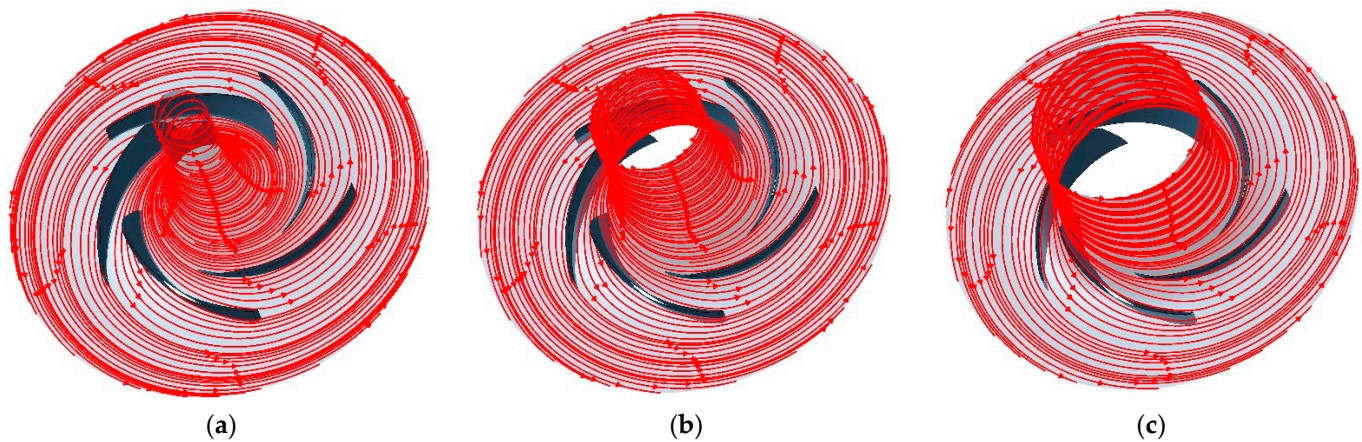


Figure 11. Relative velocity streamlines of mid-loading impeller calculated by the RANS method at 10% span (a), at 50% span (b), and at 90% span (c).

In order to measure the performance of the impeller under different working conditions, parameters such as impeller efficiency and net positive suction head available (NPSHa) are adopted. The impeller efficiency refers to the ratio of the pressure energy obtained by the fluid to the shaft power consumed by the impeller. It is an important performance index in the traditional field of pump research and is calculated as follows:

$$\eta = \frac{\Delta p_t \dot{m}}{\rho \omega T} \quad (17)$$

where Δp_t is the total pressure rise of the pump impeller, \dot{m} is the mass flow rate, ρ is the density of the fluid, and T is the torque of the impeller.

The NPSHa refers to the energy head of the unit weight liquid at the pump inlet exceeding the saturated vapor pressure at the corresponding temperature, and it is defined as:

$$\text{NPSHa} = \frac{p_{tin} - p_v}{\rho g} \quad (18)$$

where p_{tin} is the inlet total pressure and p_v is the saturated vapor pressure at the corresponding temperature.

When other conditions are constant, cavitation occurs and gradually develops as the inlet pressure decreases. However, it is difficult to occur when the inlet pressure is high.

In the next section, the analysis will focus on the performance of the three impellers when cavitation does not occur under the condition of high inlet pressure (about 150 kPa). Then, under the design speed and flow rate conditions, the inlet pressure is gradually reduced, and the cavitation resistance of the impellers is analyzed when cavitation occurs.

5.1. The Results of the Calculation with High Pressure at the Inlet

On-design performances of three AFP impellers designed based on the three loading distributions are shown in Table 3. All three design solutions meet the design requirements listed in Table 2. The shroud-loading impeller is the most efficient under the design condition. Figure 12 shows the variation of impeller efficiency with flow rate at design speed. Under off-design conditions, the impeller efficiency increases first and then decreases with increasing flow rate and reaches the maximum at the design condition. Among the impellers, the mid-loading impeller has higher efficiency under small flow conditions, the shroud-loading impeller has higher efficiency near the design point, and

the hub-loading impeller has a more balanced efficiency distribution and better performance at large flow rates.

Table 3. Performance parameters under design conditions.

	Efficiency (%)	Head (m)
Shroud-loading impeller	90.95	83.14
Mid-loading impeller	90.54	82.59
Hub-loading impeller	90.87	83.28

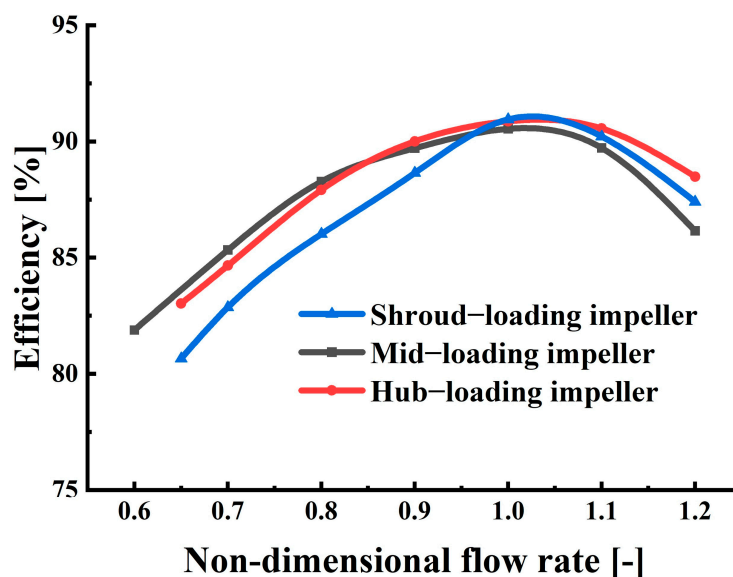


Figure 12. The variation of impeller efficiency with flow rate at design speed.

5.2. The Results of the Calculation with Low Pressure at the Inlet

In this section, the cavitation performance curves of three AFP impellers are obtained by CFD simulation under the design speed and flow condition. The results are shown in Figure 13. With a head drop of 3% as the standard, the anti-cavitation ability of the hub-loading impeller is slightly better than that of the mid-loading impeller, and the shroud-loading impeller shows the worst ability.

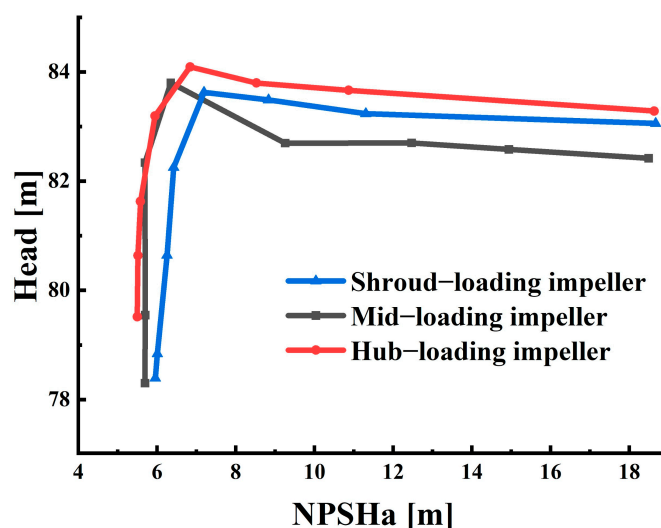


Figure 13. Head drop curves of the three AFP impellers.

From the curves of the cavitation vapor volume variation with NPSHa in Figure 14, it can be seen that when NPSHa is greater than 9 m, with the decrease of inlet pressure, the shroud-loading impeller begins to appear a slight cavitation phenomenon. This is because the suction side near the leading edge and shroud always has the lowest pressure of the flow field, which is always the first position of cavitation. The shroud-loading impeller does more work there, the pressure difference between the two sides of the blade is larger, the pressure on the suction surface is lower, and cavitation is more likely to occur. When NPSHa is less than 9 m, cavitation enters the development stage. As NPSHa decreases, the vapor volume curves of the mid-loading and shroud-loading impellers increase more obviously, while the curve of the hub-loading impeller increases more slowly. This is because the blade does more work on the hub side of the leading edge, further balancing the pressure difference of the leading edge, reducing the loading burden near the shroud, and finally improving the anti-cavitation performance of the impeller.

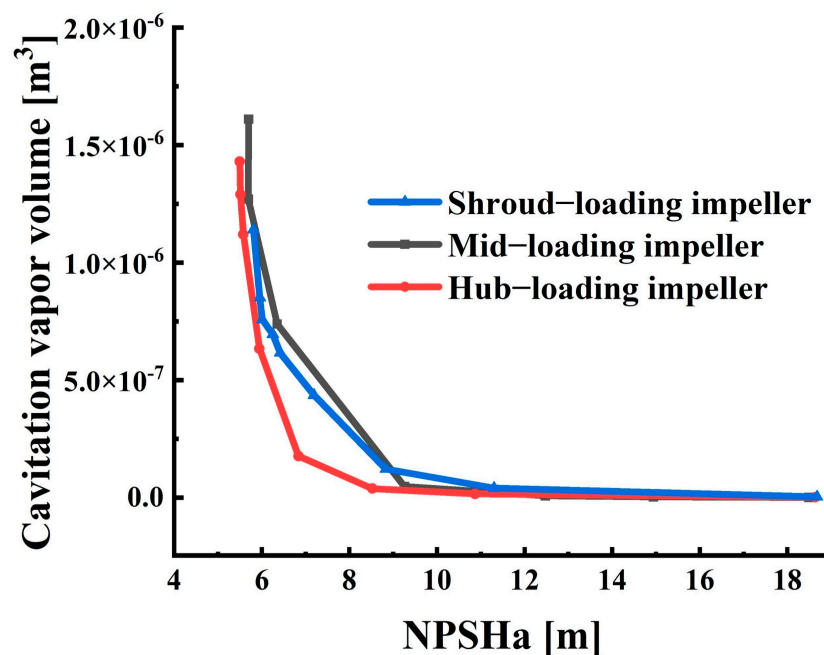


Figure 14. Cavitation vapor volume curves of three AFP impellers.

Initially, cavitation generally occurs at the suction side near the leading edge and the shroud side. Figure 15 shows the density distribution at a 90% span when the inlet total pressure is about 64 kPa. The fluid density in the area without cavitation is almost unchanged, and the density in the cavitation area decreases due to the generation of bubbles. In each figure, the upper section displays the position of the cavitation phenomenon on the entire plane, while the lower section is an enlarged view of the cavitation area. Due to the relatively less work done on the shroud side of the impeller inlet section, the cavitation area of the hub-loading impeller is the smallest, as shown in Figure 15c. In contrast, the cavitation of the shroud-loading impeller is the most serious (Figure 15a).

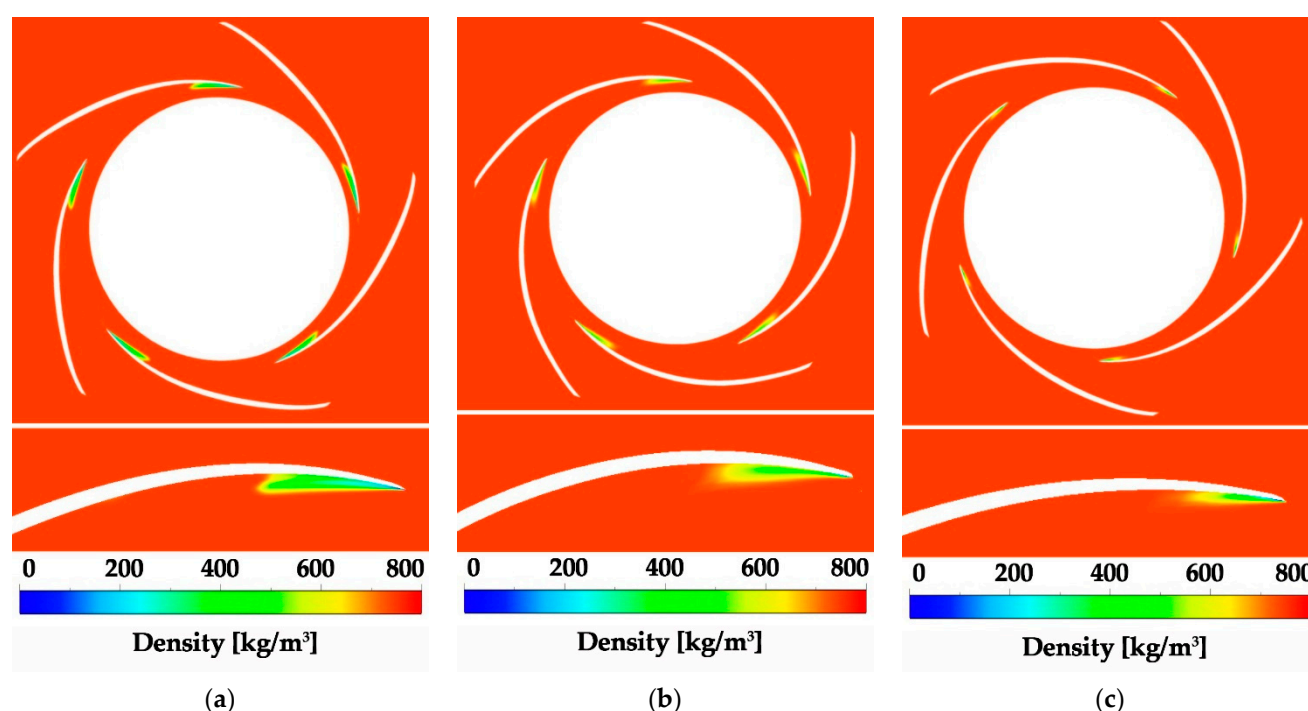


Figure 15. Density distributions at 90% span of the shroud-loading impeller (a), the mid-loading impeller (b), and the hub-loading impeller (c).

When the inlet total pressure is further reduced, the pressure on the suction side of the blade will decrease rapidly, accompanied by the rapid increase of the cavitation area. From Figures 13 and 14, it can be seen that when NPSHa decreases to a certain value, the vapor volume increases rapidly, the head decreases almost vertically, and the impeller gradually loses its ability to work. Taking the mid-loading impeller as an example, when the total inlet pressure drops to 42 kPa, the small-scale cavitation area in Figure 15b becomes a more serious cavitation that affects the performance of the entire impeller (Figure 16a), which causes the impeller head to drop by 3.15 m. The area where cavitation occurs is the low-pressure area in the blade suction side in Figure 16b. The two figures show good consistency.

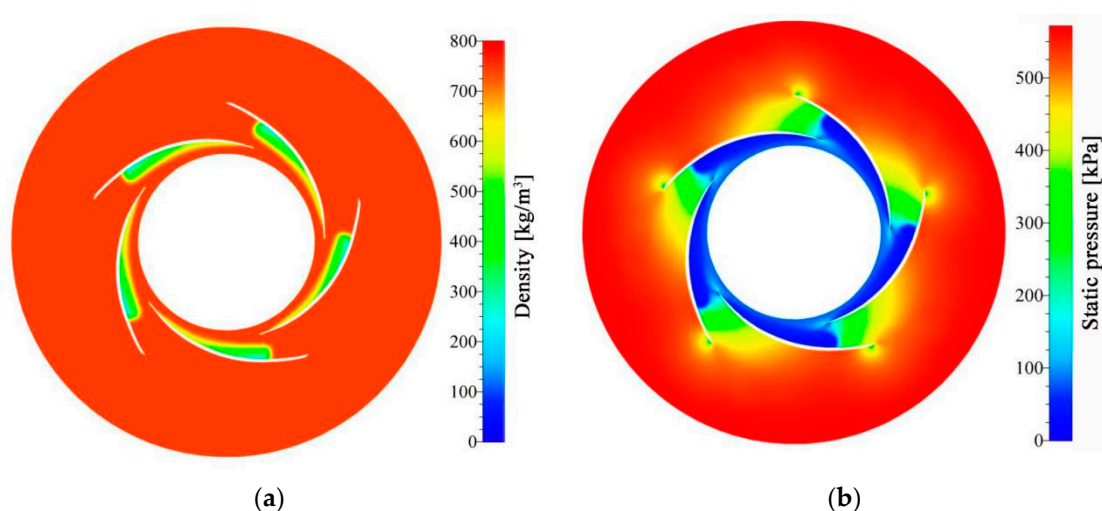


Figure 16. (a) Density distribution at 90% span of the mid-loading impeller; (b) Static pressure distribution at 90% span of the mid-loading impeller.

6. Discussion and Conclusions

In the present work, a design procedure based on the solution of an inverse problem and RANS analysis is presented, along with theory and different loading distributions. Three design strategies of the AFP impellers, based on different loading distributions, are investigated. Three different impellers' geometries are deduced by using the coupled IMDP/RANS solvers, and their performances under different working conditions are studied and compared. The following conclusions are drawn:

1. Using the inverse method can achieve the rapid design of a centrifugal impeller. The three AFP impellers designed by IMDP have good performance at the design point, and the efficiency is above 90%. The velocity and pressure of IMDP calculation are relatively consistent with RANS results, which means IMDP results have a good reference and lays the foundation for geometric design. Designers can modify the impeller according to the simulation results by adjusting the input parameters, which helps designers to get rid of the dependence on relevant databases and experience in direct design.
2. The impeller with a higher loading at the hub not only maintains a high efficiency as flow varies under the high inlet pressure conditions (cavitation does not occur) but also has better anti-cavitation performances when cavitation occurs. Hub-loading is an excellent distribution in the inverse design process.
3. The cavitation phenomena of the three impellers are different. Properly increasing the loading on the hub side of the leading edge or reducing the loading on the shroud side can suppress cavitation and effectively improve the anti-cavitation performance of the impeller. However, excessive adjustment may cause cavitation in other areas. Designers can adjust the loading near the leading edge according to the actual situation to improve the cavitation resistance.

Author Contributions: Conceptualization, C.P. and J.Y.; methodology, C.P. and J.Y.; software, C.P.; validation, C.P.; formal analysis, C.P.; investigation, C.P., J.Y. and M.F.; writing—original draft preparation, C.P.; writing—review and editing, J.Y., M.F. and Y.Z.; supervision, J.Y. All authors have read and agreed to the published version of the manuscript.

Funding: This research received no external funding.

Data Availability Statement: Additional data are proprietary and cannot be shared. Please contact the corresponding author if you want additional data.

Conflicts of Interest: The authors declare no conflicts of interest.

Nomenclature

<i>AFP</i>	aviation fuel pump
<i>CFD</i>	computational fluid dynamics
<i>IMDP</i>	inverse method design program
<i>NPSHa</i>	net positive suction head available
<i>NURBS</i>	non-uniform rational basis splines
<i>RANS</i>	Reynolds Averaged Navier–Stokes
<i>B</i>	number of blades
<i>B_f</i>	blockage factor
<i>C_p</i>	heat capacity at constant pressure
<i>f</i>	blade wrap angle
\bar{f}	average blade wrap angle
<i>g</i>	acceleration of gravity
<i>H</i>	impeller head
<i>m</i>	streamwise meridional coordinate
\dot{m}	mass flow rate

n	number of Fourier expansion terms
p^+	pressure side pressure
p^-	suction side pressure
Δp_t	total pressure rise of pump impeller
p_{tin}	inlet total pressure
p_v	saturated vapor pressure
r	radial coordinate
S	periodic sawtooth function
t_n	blade thickness
t_θ	blade tangential thickness
T	pump impeller Torque
T_{em}	temperature of the working fluid
v_{rbl}	radial periodic velocity
v_{zbl}	axial periodic velocity
$v_{\theta bl}$	tangential periodic velocity
\bar{V}_{rbl}	radial mean velocity
\bar{V}_{zbl}	axial mean velocity
\bar{V}_θ	tangential mean velocity
V_{bl}	pitchwise mean meridional velocity
W	relative velocity
z	axial coordinate
α	new angle coordinate
η	impeller efficiency
θ	angle coordinate of the cylindrical coordinate system
λ	blade load
μ_D	dynamic viscosity
ρ	density
Φ	potential function
Ψ	stream function
ω	angular velocity
$\bar{\Omega}$	vorticity

References

1. Wang, W. Research status and prospect of centrifugal aviation fuel pump. *Fluid Mach.* **2020**, *48*, 59–63.
2. Westra, R.W.; Broersma, L.; van Andel, K.; Kruijt, N.P. PIV measurements and CFD computations of secondary flow in a centrifugal pump impeller. *J. Fluids Eng.* **2010**, *132*, 061104.
3. Lorusso, M.; Capurso, T.; Torresi, M.; Fortunato, B.; Fornarelli, F.; Camporeale, S.M.; Monteriso, R. Efficient CFD evaluation of the NPSH for centrifugal pumps. *Energy Procedia* **2017**, *126*, 778–785.
4. Bozorgasareh, H.; Khalesi, J.; Jafari, M.; Gazori, H.O. Performance improvement of mixed-flow centrifugal pumps with new impeller shrouds: Numerical and experimental investigations. *Renew. Energy* **2021**, *163*, 635–648.
5. Tan, C.S.; Hawthorne, W.R.; McCune, J.E.; Wang, C. Theory of Blade Design for Large Deflections: Part II—Annular Cascades. *J. Eng. Gas Turbines Power* **1984**, *106*, 354–365.
6. Borges, J.E. A Three-Dimensional Inverse Method for Turbomachinery: Part I—Theory. *J. Turbomach.* **1990**, *112*, 346–354.
7. Borges, J.E. A Three-Dimensional Inverse Method for Turbomachinery: Part II—Experimental Verification. *J. Turbomach.* **1990**, *112*, 355–361.
8. Zangeneh, M. A compressible three-dimensional design method for radial and mixed flow turbomachinery blades. *Int. J. Numer. Methods Fluids* **1991**, *13*, 599–624.
9. Goto, A.; Zangeneh, M. Hydrodynamic design of pump diffuser using inverse design method and CFD. *J. Fluids Eng.* **2002**, *124*, 319–328.
10. Goto, A.; Nohmi, M.; Sakurai, T.; Sogawa, Y. Hydrodynamic design system for pumps based on 3-D CAD, CFD, and inverse design method. *J. Fluids Eng.* **2002**, *124*, 329–335.

11. Daneshkhan, K.; Zangeneh, M. Parametric design of a Francis turbine runner by means of a three-dimensional inverse design method. *IOP Conf. Ser. Earth Environ. Sci.* **2010**, *12*, 012058.
12. Oka, N.; Furukawa, M.; Yamada, K.; Itou, S.; Ibaraki, S.; Iwakiri, K.; Hayashi, Y. Optimum aerodynamic design of centrifugal compressor impeller using an inverse method based on meridional viscous flow analysis. In *Turbo Expo: Power for Land, Sea, and Air*; American Society of Mechanical Engineers: New York, NY, USA, 2017; Volume 50800, p. V02CT44A013.
13. Dunn, P.F.; Thomas, F.O.; Davis, M.P.; Dorofeeva, I.E. Experimental characterization of aviation-fuel cavitation. *Phys. Fluids* **2010**, *22*, 117102.
14. Gafurov, S.A.; Prokofiev, A.B.; Shakhmatov, E.V. Reduction of vibroacoustic loads in aviation combined pumps. In Proceedings of the 29th Congress of the International Council of the Aeronautical Sciences, St. Petersburg, Russia, 7–12 September 2014.
15. Gafurov, S.; Rodionov, L.; Gimadiev, A. Combined air supply at fuel pump entrance. In *Fluid Power Systems Technology*; American Society of Mechanical Engineers: New York, NY, USA, 2014; Volume 45820, p. V001T01A008.
16. Wang, W.; Li, Z. Influence of different types of volutes on centrifugal aviation fuel pump. *Adv. Mech. Eng.* **2021**, *13*, 16878140211005202.
17. Batchelor, C.K.; Batchelor, G.K. *An Introduction to Fluid Dynamics*; Cambridge University Press: Cambridge, UK, 1967.
18. Zhang, L.; Davila, G.; Zangeneh, M. Multi-objective optimization of a high specific speed centrifugal volute pump using three-dimensional inverse design coupled with computational fluid dynamics simulations. *J. Fluids Eng.* **2021**, *2*, 143.
19. Leguizamón, S.; Avellan, F. Open-source implementation and validation of a 3D inverse design method for Francis turbine runners. *Energies* **2020**, *13*, 2020.
20. Zangeneh, M.; Daneshkhan, K. A fast 3D inverse design based multi-objective optimization strategy for design of pumps. *Fluids Eng. Div. Summer Meet.* **2009**, 43727, 425–431.
21. Xiong, Y. *Analysis and Optimization of Cavitation Performance of an Aviation Fuel Pump*; Beijing Institute of Technology: Beijing, China, 2016.
22. Pouffary, B.; Fortes-Patella, R.; Reboud J.L.; Lambert, P.A. Numerical Simulation of 3D Cavitating Flows: Analysis of Cavitation Head Drop in Turbomachinery. In Proceedings of the 2005 ASME Fluids Engineering Division Summer Meeting and Exhibition, Fifth International Symposium on Pumping Machinery, Houston, TX, USA, 19–23 June 2005.

Disclaimer/Publisher’s Note: The statements, opinions and data contained in all publications are solely those of the individual author(s) and contributor(s) and not of MDPI and/or the editor(s). MDPI and/or the editor(s) disclaim responsibility for any injury to people or property resulting from any ideas, methods, instructions or products referred to in the content.